Metallomics

Dynamic Article Links

Cite this: *Metallomics*, 2012, **4**, 156–165

www.rsc.org/metallomics

PAPER

Zn induced structural aggregation patterns of β-amyloid peptides by first-principle simulations and XAS measurements

Paolo Giannozzi,[a] Karl Jansen,[b] Giovanni La Penna,*[c] Velia Minicozzi,[d] Silvia Morante,[d] Giancarlo Rossi[d] and Francesco Stellato[e]

Received 1st September 2011, Accepted 25th November 2011
DOI: 10.1039/c2mt00148a

We show in this paper that in the presence of Zn ions a peculiar structural aggregation pattern of β-amyloid peptides in which metal ions are sequentially coordinated to either three or four histidines of nearby peptides is favored. To stabilize this configuration a deprotonated imidazole ring from one of the histidines forms a bridge connecting two adjacent Zn ions. Though present in zeolite imidazolate frameworks, remarkably in biological compounds this peculiar Zn–imidazolate–Zn topology is only found in enzymes belonging to the Cu,Zn-superoxide dismutase family in the form of an imidazolate bridging Cu and Zn. The results we present are obtained by combining X-ray absorption spectroscopy experimental data with detailed first-principle molecular dynamics simulations.

1 Introduction

Alzheimer's disease (AD) belongs to a family of heterogeneous pathologies (more than 20), generically termed amyloidosis, in which endogenous proteins and/or peptides switch from the physiological soluble configuration to a pathological fibrillar insoluble state.[1,2]

It is generally believed that metals play an important role in the development of the disease on the basis of the observation that senile plaques in AD patients have been generally found to display an increased concentration of transition metals (with Cu, Zn and Fe being the most abundant).[3,4] Moreover there is solid evidence that a breakdown in metal trafficking regulation has a significant impact on the development of age-related neurodegenerative pathologies.[5,6]

Cu and Zn have been the most studied metal ions (see ref. 7–9 and references therein). Their relevance has been also confirmed by the experimental observation that treatment with Cu and Zn chelators inhibits accumulation of β-amyloid (Aβ) peptides which are the main proteinaceous components of the amyloid brain deposition detected in AD patients.[10] A further interesting fact is that Zn is seen to induce Aβ aggregation more effectively than Cu.[11,12]

From a structural point of view to date most of the experimental results[13,14] and numerical simulations[15,16] converge on the conclusion of a stable intra-molecular Cu coordination. The situation appears to be much more complicated for Zn^{2+}–Aβ-peptide complexes, and several Zn^{2+} coordination modes have been proposed.[17–19]

Recent EPR data (see ref. 20 and references therein) and XAS[21] measurements, carried out in the related case of the prion protein, have shown that there is a competition for peptide binding between the two ions, thus suggesting the existence of a mechanism for fine regulation of metal binding to prevent cell damage.

In this general framework it appears to be of the utmost importance to understand and clarify whether and how Cu^{2+} and Zn^{2+} differ in their way of interacting with amyloidogenic peptides in general, and Aβ-peptides in particular.[21]

For Zn, NMR investigations[13] have suggested a variety of inter-molecular metal binding modes involving, besides other ligands, different numbers of histidines. The existence of peculiar inter-molecular binding modes was confirmed by a XAS study of the Zn^{2+}–Aβ(13–21) complex[22] in which pairs of peptides appear to be cross-linked by a Zn^{2+} bridge binding two histidines belonging to different peptides. In more recent NMR studies also intra-peptide coordination modes in which Zn^{2+} binds three histidines and either the N-terminus[19] or the Glu_{11} residue,[23] have been proposed. The variability of Zn^{2+} coordination modes (according to *e.g.* concentration, sample preparation, *etc.*) was also confirmed by XAS data on the Zn^{2+}–Aβ(1–40) complex.[7,8] The structure suggested by XAS analysis showed a high histidine crowding around Zn, with at

[a] *University of Udine, Department of Chemistry, Physics and Environment, via del Cotonificio 108, 33100 Udine, Italy*
[b] *John von Neumann Institute for Computing—DESY Zeuthen, Platanen allee 6, 15738 Zeuthen, Germany*
[c] *National Research Council, Institute for Chemistry of Organo-metallic Compounds, via Madonna del Piano 10, 50019 Sesto fiorentino (Firenze), Italy. E-mail: glapenna@iccom.cnr.it; Fax: +39 0555225203; Tel: +39 0555225264*
[d] *Department of Physics, University of Roma "Tor Vergata" and National Institute of Nuclear Physics, Section of Roma "Tor Vergata", via della Ricerca Scientifica, 00133 Roma, Italy*
[e] *Centre for Free-Electron Laser Science—DESY, Notkestrasse 85, 22607 Hamburg, Germany*

least three His sidechains coordinated to Zn. In order to reach a definite conclusion about the Zn coordination the local structural information extracted from XAS experiments had to be complemented with other spectroscopical and biochemical data. The four-histidines Zn coordination was found compatible with all the available data, while the three-histidines coordination was excluded (see the discussion in ref. 8). Since along the Aβ-peptide sequence only three histidines are present, this geometrical arrangement hints at a Zn^{2+}-promoted inter-peptide aggregation mode. A four-histidines Zn binding mode, like the one described above, is rather peculiar as it was not described among proteins endowed with a mononuclear Zn site before 2003.[24] A recent survey of metal ion coordination in the PDB[25] found one case of Zn coordination to four His sidechains belonging to the same protein monomer (PDB code 1PB0[26]) over 5854 PDB entries containing at least one Zn atom. One other case of Zn coordination by four His sidechains involves sidechains belonging to different monomers (the dinuclear heme activator protein HAP1, and PDB codes 1HWT and 1QP9[27]).

Another peculiarity of Zn–Aβ-peptide binding is that experimental data suggest that the four involved histidines are the two consecutive His_{13} and His_{14} residue pairs coming from two nearby Aβ-peptides. This is a very special arrangement as structural databases report one single instance where a metal (actually Cu) is bound to two histidines that are one next to the other along the protein sequence.[28]

There are instead many cases where Cu is coordinated to four histidine sidechains belonging to the same monomer, but all of them concern proteins belonging to the wide class of Cu,Zn-superoxide dismutases (Cu,Zn-SOD). Actually a fully Zn-substituted Cu,Zn-SOD enzyme (encoded by the human SOD1 gene) has been shown to be at least as stable as the wild-type heterodinuclear protein.[29]

The coordination of Zn by four neutral imidazolyl groups is infrequent even within non-protein coordination complexes. A search for this coordination in the Cambridge structural database (CSD)[30] yields, with the exception of tetraimidazole Zn^{2+} perchlorate,[31] only structures in which the imidazolyl group is either deprotonated (imidazolate) or *N*-methyl protected. In the first case each imidazolate group coordinates two Zn ions (see CSD code IMIDZB01[32]) leading to the formation of an extended network, a process that indeed can only be prevented by N-methylation.

Recently the special properties of Zn–imidazolate–Zn bridge topology have found a wide area of applications in the zeolite imidazolate frameworks (ZIF).[33] ZIF structure is reminiscent of that of zeolites, with zinc and imidazolate in the former taking approximately the positions that aluminium and silicate have in the latter. In both cases extended, regular and stable structures with large cavities are formed. Noticeably, Zn–imidazolate compounds can be obtained in the presence of weak bases, like dimethyl-formammide, thus showing that the acidity of NH in the imidazolyl group is assisted by the formation of the Zn–imidazolate aggregate.

One might be tempted to conclude that the peculiar Zn binding mode suggested by recent experimental data is a hallmark of peptide aggregation. Although they certainly give a significant indication in this direction, XAS data alone are not enough to reach such a conclusion. In fact, it is certainly true that the strength of XAS resides in its sensitivity to short range order as it allows us to reliably identify at atomic resolution the average structure around the metal absorber for systems in any state of aggregation. But the limitations of this spectroscopy are precisely that the structural information one can get is what results from averaging over the different possibly existing structures in which the metal absorber may be coordinated and is furthermore confined to within a sphere of a few Angstroms around the absorber (say 5–6 Å). On the other hand, in order to fully understand the complicated peptide aggregation mechanism assisted by metals, one must be able to reconstruct the structure of the system at distances larger than 6 Å from the absorber, as it looks that a large oligomeric or polymeric structure gets formed.

In this work we show that the configurations of the Zn–Aβ complexes that are able to simultaneously fit the experimental findings (see ref. 8) and the results coming from numerical simulations are quite complicated. Aβ-peptides are cross-linked by Zn ions, with one Zn bonded by two pairs of adjacent histidines (His_{13} and His_{14}) from two peptides, and a second Zn is necessary to stabilize the system, replacing the proton in the NH group of one of the involved imidazolyl sidechains. This pattern can repeat itself thus including a large number of monomers. Indeed, our extensive first-principle (Car–Parrinello molecular dynamics) and semi-empirical (tight-binding methods and Born–Oppenheimer molecular dynamics) combined simulations support the picture of a Zn-assisted deprotonation of (at least) one of the histidine sidechains of the peptide in the formation of aggregated complexes.

2 Methods

In this section we describe the construction of the four models of Aβ-peptide–Zn complexes we have built to fit the experimental XAS data. The construction is based on general structural information and more or less sophisticated numerical methods (ranging from empirical modeling of single and multiple peptide compounds to small truncated first-principle simulations, the latter being dealt with at the level of the density functional theory). The geometry of the resulting metal site is optimized (*i.e.* fitted) against the available XAS data. The $\chi(k)$ data are fitted employing the EXCURV98 package.[34]

The necessity of using this two-fold strategy (*i.e.* large scale modeling plus data fitting) comes from the fact that we do not simply want to reproduce Zn-K-edge XAS spectra (for which, as we said, the knowledge of the atomic geometry in a small sphere of radius, say, 5–6 Å is enough), but we also want to identify stable Zn–Aβ-peptide organized structures (for which the knowledge of the geometry of the sample at large is required). This is necessary in order to be able to answer the key question of whether and how Zn can promote the first steps of Aβ-peptide aggregation processes.

The starting point of all the successive modeling steps is the construction, through interactive molecular manipulations performed with the VMD graphical interface,[35] of configurations of a complex formed by two Aβ(1–16) chains plus a Zn^{2+} ion.

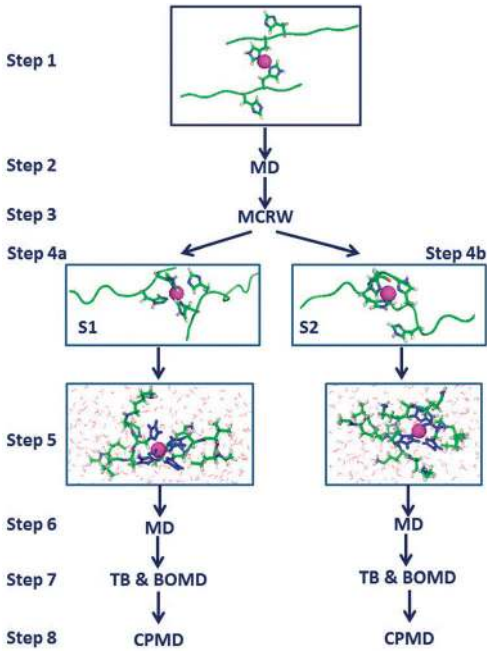

Fig. 1 Flow-chart of the construction of models S1 and S2. See text for the meaning of symbols and details.

The two identical Aβ(1–16) chains, with charged N- and C-termini, were designed (see Fig. 1, Step 1) with Φ and Ψ backbone dihedral angles set at 180° and the other geometrical parameters taken from standard amino acid geometries. As shown in the figure, the two Aβ chains, from now on referred to as chain A and B, respectively, are assembled in an antiparallel way with the two Nδ atoms of $His_{14}^{(A)}$ and $His_{14}^{(B)}$ bonded to a single Zn atom. The energy of this initial configuration, computed with the empirical PARM94 Amber force-field[36] (as for the protein) and the parameters reported in ref. 17 and 37 (as for the Zn coordination), was minimized using the program NAMD[38] (see Fig. 1, Step 2).

To relax the above structure a Monte Carlo random walk[39] (MCRW) was used, where all the dihedral angles in the two peptide chains were randomly changed (Step 3), with the exception of those belonging to the two His_{14} sidechains that were held fixed to keep the Nδ($His_{14}^{(A)}$)–Zn–Nδ($His_{14}^{(B)}$) motif blocked in space. The virtue of this random walk sampling is that no configurations of the Zn-bridging dimer with "bad" contacts between pairs of atoms are ever accepted.†

Along the trajectory, one particular configuration (model S1, see Step 4a) was picked up in which Zn is closer than 3 Å from the Nε of His_{13} in both monomers. The reason for this choice is that among the others the resulting four-fold Nε($His_{13}^{(A)}$)–Nδ($His_{14}^{(A)}$)–Nε($His_{13}^{(B)}$)–Nδ($His_{14}^{(B)}$) Zn-coordination‡ is, according to NMR data[23] and Car–Parrinello (CP-MD) simulations,[17] the most stable one.

A second model (S2 in the following) was constructed where Zn is coordinated to three histidine imidazole rings (instead of four, as in S1) in a 3N1O configuration (with the oxygen coming from the main chain of one of the bound histidines). This model was built to test whether a three-imidazole Zn geometry can be a valid alternative to the four-imidazole Zn coordination mode advocated in the literature to explain and fit the spectral features of the XAS Zn–Aβ data.[8] The construction of model S2 went on in the following way. Among the set of configurations produced by MCRW, one in which Zn is coordinated to Nδ of $His_{13}^{(A)}$, $His_{14}^{(A)}$, $His_{14}^{(B)}$ and O of $His_{14}^{(A)}$, was selected (Step 4b).§ The reason for binding the oxygen of His_{14} is that the resulting geometry mimics a sort of "half-histidine" structure in the sense that from the XAS point of view only half of the pathways available to the photo-electron compared to the situation in which the metal is bound to an imidazole ring are now allowed.

The Zn-bridged Aβ(1–16) dimers (S1 and S2) built as we explained, were truncated down to models affordable by semi-empirical and first–principle methods (Step 5). In particular the segments 1–10 of both peptide chains were removed and the Glu_{11} N-terminal was capped with the usual acetyl group.

Then the standard minimization of energy in the empirical force-field was performed (Step 6).

Each truncated dimer was merged into an orthorhombic cell whose dimensions were determined in order for the periodic replicas to be separated by 0.5 nm. The cell is filled with 376 TIP3P[40] water molecules. The water is thermalized and brought to 300 K increasing the temperature in steps of 100 K from 0 K to 300 K by four empirical MD trajectories of 10 ps each.[41] During the thermalization procedure peptide and Zn atoms were kept fixed in space. In the last 300 K step the pressure was held constant at 1 bar (compressibility of bulk water at room conditions was used).

The final solvated configurations obtained in Step 6 were then subjected to the tight-binding semi-empirical (TB) calculations[42] described below to further relax the whole system. TB calculations were performed by employing the density functional tight-binding method implemented in the DFTB+ code.[42] The parameters for organic compounds containing Zn were used.[43] The Γ-point condition ($K = 0$) was adopted in all the electronic structure calculations. After energy minimization, to bring the system at room temperature a first constant energy Born–Oppenheimer MD (BO-MD) simulation step of 200 fs was performed, which led the system to an average temperature of 46 ± 4 K. The system was progressively heated up to the desired temperature of 300 K by using the same type of thermostat of the empirical MD simulations[41] (Step 7). At each temperature BO-MD simulations were carried out for 200 fs with a time-step of 1 fs.

Since, as also suggested by the analysis of XAS data, Zn is *preferably* penta-coordinated, the oxygen of a water molecule is brought at a binding distance from the metal as a fifth Zn ligand. The resulting configurations of the S1 and S2 models were finally subjected to a full quantum-mechanical step using CP-MD[44] (Step 8) in order to check for the stability of the Zn

† In the system we are considering, which has 124 dihedral angles, the number of attempted torsional moves was 10^6, with an acceptance rate of about 1/2.

‡ Recall that the Nδ ($His_{14}^{(A)}$)-Zn-Nδ ($His_{14}^{(B)}$) motif was held fixed in the MCRW step.

§ The Nδ coordination is comparatively more frequent in MCRW because, when a histidine detaches, it rebinds the Zn preferably *via* Nδ.

coordination. It is indeed a well recognized fact that classically unnoticed instabilities are easily spotted and amplified to a visible magnitude by even very short (of the order of a few picoseconds) quantum-mechanical simulations of the CP-MD type.[45] From now on, with the word stability we mean the resistance of Zn coordination to thermal fluctuations at room conditions (liquid water at $T = 300$ K).

To carry out the necessary quantum-mechanical CP-MD simulations, the parallel version of the Quantum ESPRESSO package,[46] which incorporates Vanderbilt ultra-soft pseudopotentials[47,48] and the Perdew–Burke–Ernzerhof exchange correlation functional,[49] was employed. Electronic wave functions were expanded in plane waves up to an energy cutoff of 25 Ry, while a 250 Ry cutoff was used for the expansion of the augmented charge density in the proximity of the atoms, as required in the ultrasoft pseudopotential scheme.[49] Simulations were carried out according to the general protocol described in ref. 50.

A third model, S3, was designed, slightly modifying model S1, by substituting the Hε atom of $His_{14}^{(A)}$ with a second Zn ion. In the following we will refer to the two Zn atoms as Zn_a and Zn_b. Zn_b is bound to the Nε of $His_{14}^{(A)}$ and two oxygens from the Glu_{11} sidechain. To keep the system in the CP-MD simulation cell neutral, one water molecule, relatively far from the peptide, was replaced by a chlorine atom.

A final fourth model, S4, is obtained by adding a third peptide fragment (chain C, truncated down to a 11–16 fragment, as it was done for chains A and B), with Nε ($His_{13}^{(C)}$) and Nδ ($His_{14}^{(C)}$) atoms in the same positions as the two water molecules that are bound to the second Zn site (Zn_b site) in model S3 at the end of CP-MD simulation (see Table 1 in the Results section). Since the whole system is now neutral, the chlorine atom is removed from bulk water. The two systems were successively slowly heated up to 300 K using the same TB and BO-MD steps described above for S1 and S2 (see Fig. 1, Step 7). Due to the impossible large dimension of system S4, only S3 has been subjected to CP-MD simulations (Step 8).

In Fig. 2 for the reader's convenience we summarize how, in the four different models we have described, Zn ions are bound to the histidines of the various Aβ monomers successively coming into play.

Table 1 For each system in the first column, we report in the second column the atoms that lie within 2.5 Å from Zn (*i.e.* inside the Zn-coordination shell) before the CP-MD or BO-MD simulations. The subscripts (His, Glu, W) denote the residue/molecule to which the atom belongs (W stands for water). In S3 and S4 models the two Zn atoms are indicated by Zn_a and Zn_b. In the third and fourth columns the structural variations observed at the end of the simulations at temperatures up to 250 K and at 300 K, respectively, are reported. "Minus" indicates that a ligand leaves the Zn coordination sphere, while "plus" that it enters it

		Zn-binding modification	
Name	Starting configuration	0–250 K	300 K
S1	Zn: $4N_{His} + 1O_W$	$-1N_{His}$	None
S2	Zn: $3N_{His} + 1O_{His} + 1O_W$	$-1O_{His}$	None
S3	Zn_a: $4N_{His} + 1O_W$ Zn_b: $1N_{His} + 2O_{Glu}$	Zn_b: $+1O_W$	Zn_b: $-1O_{Glu} + 1O_W$
S4	Zn_a: $4N_{His} + 1O_W$ Zn_b: $3N_{His} + 1O_{Glu}$	None	None

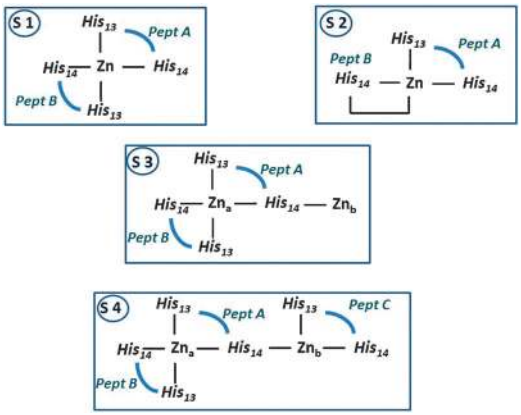

Fig. 2 A schematic view of the Zn site in the four models we have constructed. Histidines connected by blue bands belong to the same peptide. The staple comprising His_{14} and Zn in the S2 model is there to recall that, besides three *imidazoles*, the oxygen of the His_{14} main chain is also bound to the metal.

3 Results

The salient features of the evolution of the S1, S2, S3 and S4 model configurations in the long process of system construction and thermalization are summarized in the flow-chart of Fig. 1 and Table 1, respectively.

In the second column of Table 1 (starting configuration) we list the Zn coordination modes of the four systems before the CP-MD (for models S1, S2 and S3) and BO-MD (for model S4) simulations. At the beginning of these last simulation steps, Zn in model S1 and Zn_a in models S3 and S4 are coordinated to four nitrogens (from four histidines) and one oxygen from a water molecule. In model S2, Zn is coordinated to three nitrogen from three histidines, one oxygen from a water molecule and a second oxygen from the main chain of $His_{14}^{(A)}$. In model S3, an extra Zn, denoted by Zn_b, is added solely to check whether its presence is able to stabilize the four histidine coordination of Zn_a. It is coordinated to one nitrogen from the histidine bridging the two Zn ions and two oxygens from the Glu_{11} sidechain. In model S4, which is intended to represent a hypothetic, perhaps more realistic situation, a third peptide chain is added to stabilize the whole compound. In this system Zn_b is coordinated to three nitrogens from three histidines and one oxygen from Glu_{11}. These four "starting" configurations are depicted in the left column of Fig. 3.

The structural modifications that occur when we perform the last CP-MD (for models S1, S2 and S3) and BO-MD (for model S4) simulation steps are summarized in the third and fourth columns of Table 1.

Heating the systems from 0 to 250 K (third column), one notices that both in the S1 and S2 models Zn loses one ligand and ends up in a tetrahedral 3N1O coordination. In fact, it loses the nitrogen of a histidine in the case of S1 and the oxygen of His_{14} in the case of S2. For what concerns model S3, it is very remarkable that the unlikely three-fold coordination of the extra Zn_b readily becomes a more realistic tetra-coordination owing to the oxygen of a water molecule that is attracted within its coordination shell (2.5 Å). Interestingly enough the Zn coordination of both metal sites in model S4 remains unchanged.

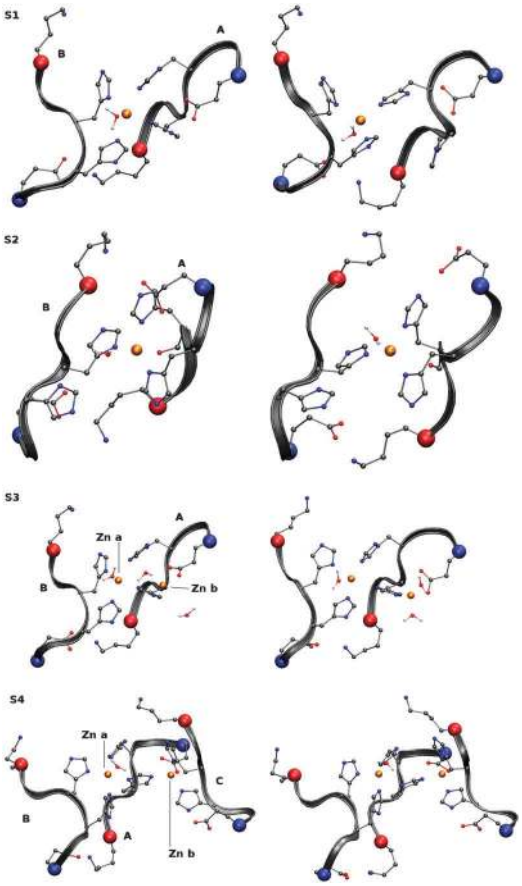

Fig. 3 Left column: starting (energy minimized) configurations of models S1, S2, S3 and S4 (from top to bottom). Right column: final configurations (at 300 K) after CP-MD (for models S1, S2 and S3) and BO-MD (for model S4) simulation steps. Zn atoms are shown in orange. Only His, Glu and Lys sidechains are displayed. Blue and red spheres refer to Cα atoms of N- and C-termini, respectively. H atoms are not displayed, except when they belong to water molecules. The VMD program[35] was employed for molecular manipulations and drawings.

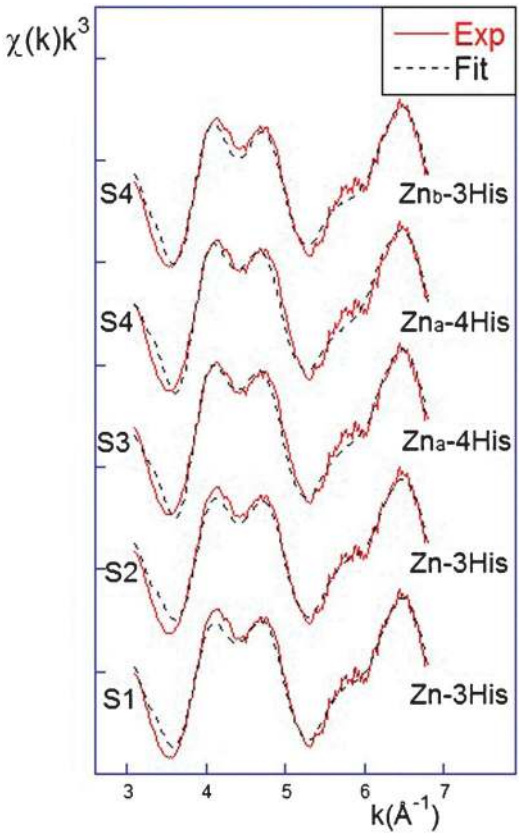

Fig. 4 Experimental (red full line) and fitted (black dotted line) XAS data. The analysis of XAS data is made by starting with the fitting geometry obtained at the end of CPMD (or BO-MD) simulation steps. The fit to the uninteresting (see text) Zn_b one histidine site in model S3 is not reported.

In the last column, we report the final modifications that take place when the systems are brought to room temperature. We see that the only thing that happens is that in model S3 one of the two Zn_b coordinated Glu_{11} oxygens is replaced by the oxygen of a second water molecule attracted in the coordination shell.

In Fig. 3 the configurations before (left panel) and after (right panel) the last CP-MD (for models S1, S2 and S3) and BO-MD (for model S4) simulation steps are compared.

All the final models shown in the right column of Fig. 3 (see the last column of Table 1) have been tested against XAS data by fitting their geometrical parameters.¶ The results are reported in Fig. 4 where the red solid line represents the experimental spectrum (common to all panels) and the dotted black lines represent the fitted curves. The results of the fits to the Zn_b site in the S3 model, where the metal is coordinated to one histidine, have not been reported. Indeed since this extra Zn was only introduced to stabilize the S3 tetrahedral Zn_a coordination, its coordination mode is of not much structural interest.

The comparison displayed in Fig. 4 shows that different models with either three or four Zn-coordinated histidines can be constructed which are able to satisfactorily fit the XAS data of ref. 8. This finding shows that XAS data alone are not enough to fully resolve the metal site coordination structure. Indeed, in ref. 8 besides XAS data a number of other spectroscopic information were used to elucidate this issue. Here we show that numerical simulations can be employed to uniquely identify stable metal–Aβ-peptide configurations, which also allow us to determine the long-range molecular arrangement of the system.

In order to explore possible effects of the detected long-range coordination topology on the structure within the 1–10 residue region of Aβ peptides identified in the various first-principle and semiempirical approaches described above, empirical models including the entire 1–16 regions of the three peptide chains of models S1, S2 and S4 were also simulated at $T = 300$ K. The structure of the 11–16 region, as well as the positions of the Zn atoms, were kept fixed as they appear in the final configuration displayed on the right hand side of Fig. 3. In Fig. 5 (left) the initial configurations (with the whole 1–10 regions in the all-trans configuration attached to the corresponding 11–16 peptides) of S1, S2 and S4 models are

¶ Note that concerning the initial geometry of the four models we used for XAS data fitting, we have actually taken the configuration obtained after a further minimization step intended to bring the simulated system nearer to the actual experimental conditions where samples were frozen down to 20 K (liquid nitrogen).

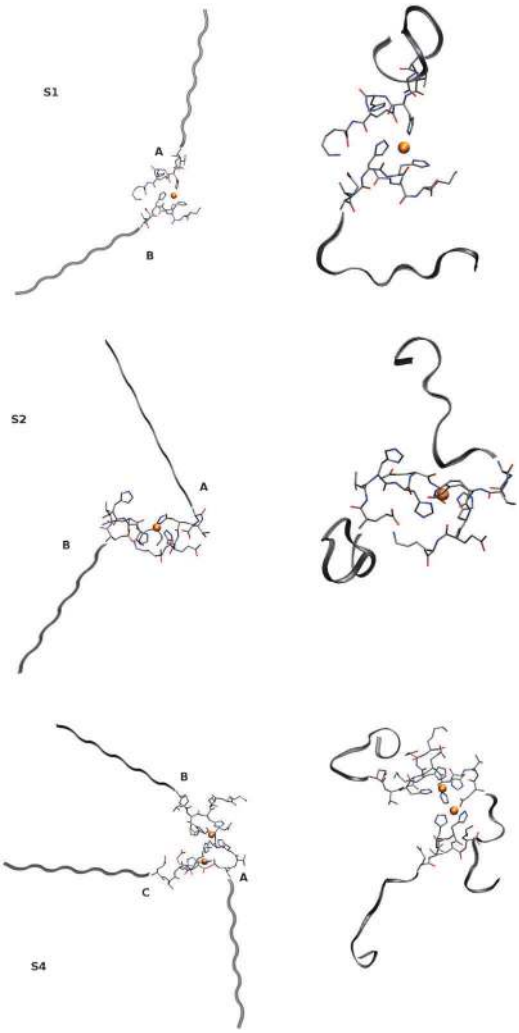

Fig. 5 Starting (left panel) all-trans N-termini configurations and final (right panel) MD configurations at $T = 300$ K, after $t = 10$ ps, for models S1, S2 and S4, extended to full Aβ (1–16) peptides (see text for details). Zn atoms are displayed in orange, atoms in the 11–16 regions are displayed with sticks, hydrogen atoms are not shown. N-termini are represented as ribbons.

displayed, and are compared (right) with the configurations obtained after a 10 ps classical simulation. All simulations were carried out in vacuum and with a small cut-off (0.5 nm) for non-bonding interactions to prevent unphysical much too large hydrophobic forces.

Comparison of the final structures one obtains for the three models is fairly interesting. It clearly shows that in models S1 and S2 the probability of mutual interactions between chains A and B is low, while the 1–10 residue regions have more chances to collapse onto the Zn-jointed 11–16 regions of the corresponding chain. In contrast, in model S4 the chance of interactions is enhanced by the N-terminal chain crowding (three chains instead of two) and the relative positions of chains A and C. In order to get more insight on the S4 model, the configuration displayed in Fig. 5 bottom-right was merged into an orthorhombic box of 1739 empirical water molecules (see Methods) and simulated for 500 ps at $T = 300$ K. This more detailed empirical model confirms what was found in

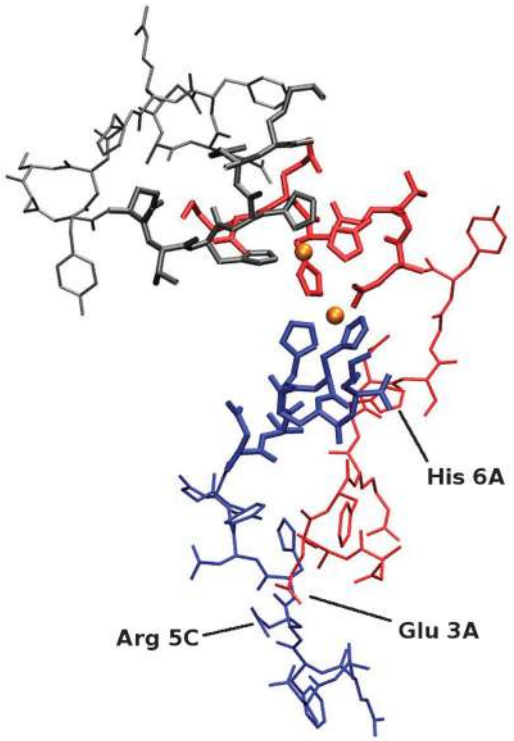

Fig. 6 Final MD ($t = 500$ ps, $T = 300$ K) configuration of the S4 model extended to the full Aβ (1–16) peptide, solvated in water (see text for details). Zn atoms are displayed in orange, atoms are displayed with sticks, hydrogen atoms are not shown. Chain A is in red, B is in gray and C is in blue. Bonds in the 11–16 residue regions are thicker than those in the 1–10 regions.

vacuum, namely that quite strong interactions, persistent for the whole duration of the simulation, are able to stabilize the mutual wrapping of chains A and C.

The configuration obtained after 500 ps at $T = 300$ K is displayed in Fig. 6, with the same orientation as in Fig. 5 bottom-right. The mutual arrangement of chains A and C shows a propensity for a sort of double helix, where the two 1–10 regions are extended left-handed helices, and slightly shifted along the sequence. Each residue in chain A is approximately facing a next sequence residue of chain C. This arrangement, induced by the mutual orientation of the 11–16 regions in chains A and C, is imposed by Zn coordination, and it is sealed by the stable salt-bridge between $Arg_5^{(C)}$ and $Glu_3^{(A)}$ ($C\zeta$ ($Arg_5^{(C)}$)–$C\delta$ ($Glu_3^{(A)}$) = 3.7 ± 0.3 Å), in turn helped by the sequence shift between the two chains. Interestingly, always as a consequence of this residue sequence shift, $N\delta$ ($His_6^{(A)}$) comes out to be relatively close to Zn_b (6 Å on average, with a minimal value of 3.6 Å), thus indicating a possible further mechanism pointing to an increase of Zn induced histidine crowding propensity.

4 Discussion

In this section, we will discuss in more detail the interactions stabilizing the crowding of histidine sidechains around Zn in the models we have proposed.

Let us start by examining how the structure of the S1, S3 and S4 models have "evolved" along their construction history.

We do not discuss S2 as in this model Zn is coordinated to only three histidines. Naturally a special attention will be devoted to what happened at the end of the simulations (either CP-MD or BO-MD), *i.e.* when the systems are brought to room temperature.

In the case of the S1 model, the initial (step 1, Fig. 1) antiparallel orientation of the two peptides making the dimer is largely relaxed already in the first empirical (MD and MCRW) simulation runs. Further important structural modifications occur during the final CP-MD step. In fact, comparing the S1 structures (first row of Fig. 3) at the beginning (left) and at the end (right) of the simulation, one notices that, although the salt-bridge between $Lys_{16}^{(A)}$ and $Glu_{11}^{(B)}$ sidechains is maintained throughout the whole simulation, the salt-bridge between the opposite termini ($Lys_{16}^{(B)}$–$Glu_{11}^{(A)}$) never forms. The reason is that, due to the distortion of the peptide chain forced by the Zn binding to two adjacent histidines, only one of the two possible salt-bridges can form. But the key feature of this model is that the bond between $His_{14}^{(A)}$ and Zn is broken during the first stage of the CP-MD thermalization (see Table 1) leaving a three histidine coordinated Zn. Most probably in the breaking of the $His_{14}^{(A)}$ bond an important role is played by $Glu_{11}^{(A)}$, since the latter remains very near to the Hε of $His_{14}^{(A)}$ throughout the whole CP-MD simulation (first row from top of Fig. 3). This information definitely could have not been inferred from XAS data alone.

To try to repair this undesired feature, in model S3 a second Zn was added. As one can see from Table 1, Zn_a remains coordinated to four histidine sidechains. Furthermore, unlike the case of S1 discussed above, $Glu_{11}^{(A)}$ now forms a stable bond with Zn_b, thus reducing its interaction with $His_{14}^{(A)}$ and the propensity to form a salt-bridge with $Lys_{16}^{(B)}$.

The resulting Zn_a and Zn_b coordination modes are rather different. As we said, Zn_a remains coordinated to four histidine sidechains, while Zn_b is coordinated to one histidine and a glutamic acid. Such a coordination would not provide a good fit to XAS spectral data, as the measured XAS signal is determined by the "effective (average) number" of histidine per Zn ion (in this case something between 2 and 2.5).

In model S4 a third peptide chain, besides the extra Zn_b, is introduced. Now both the $Lys_{16}^{(A)}$–$Glu_{11}^{(B)}$ salt-bridge (as in models S1 and S3) and the Zn_b–$Glu_{11}^{(A)}$ bond (as in model S3) are formed. Furthermore, we notice that $Glu_{11}^{(A)}$ remains in proximity of $Lys_{16}^{(C)}$.

By analyzing the S4 model configuration evolution during the TB BO-MD simulation at 300 K, one notices that the Zn_a–His–Zn_b bridge favors a stable topology for oligomeric assemblies, in which the three peptides are significantly rotated with respect to the initial antiparallel arrangement (see the bottom-right snapshot in Fig. 3 and the bottom of Fig. 5). The Zn_a–His–Zn_b bridge, while allowing the binding of $Glu_{11}^{(A)}$ sidechain to the second Zn_b ion, forbids the formation of the $Lys_{16}^{(B)}$–$Glu_{11}^{(A)}$ salt-bridge but, at variance with what happens in the S1 case, an array of $Glu_{11}^{(X)} - Lys_{16}^{(X')}$ salt-bridges can be easily formed, without significant distortion of the Zn_a four-histidine sidechain coordination.

The stability of the S4 system is related on the one hand to the formation of a Zn–His–Zn bridge assisted by a deprotonated imidazole ring (imidazolate), and on the other hand to the large angle occurring between peptides A and C when the peptide B is intercalated between the two. This angle is in fact definitely larger than that formed by chains A and B when they are interacting with a single Zn ion (like in models S1 and S2). This intercalated structure "survives" the BO-MD simulation at 300 K owing to the formation of a $Glu_{11}^{(A)}$–Zn_b binding with Zn_b forcing the necessary arrangement of the His_{13}–His_{14} pair of peptide C within the Zn coordination sphere.

Naturally a crucial test of the phenomenological reliability of the models we have constructed is their ability of reproducing the key features of the XAS spectral data. As we have already said at the end of the previous section, the salient features of the XAS spectrum are better fitted by the S4 model where Zn is coordinated to four histidines in site *a* and three in site *b*.

A side observation may be appropriate here. One might suspect that in the fitting process the geometry of the tested models is somewhat altered with respect to the structure emerging from our simulation procedure, from which the fit is started. This is not so, however. As an example we show in Fig. 7 the atomic structure of the Zn_a site of the S4 model as it comes out of the fit (in green) compared to the S4 configuration just before the fit. We notice that the location and the orientation of the four histidine sidechains are almost identical in the two structures, meaning that only minor adjustments in the geometrical parameters were necessary to fit XAS data.

The conditions for deprotonation of the histidine sidechain in peptides and proteins have been the object of investigations since a long time. *In vivo* it has been observed that mild acidic conditions (pH ≈ 6.6) accompany Alzheimer's disease.[51] Aβ(1–42) has a negative charge at physiological pH (~7), mainly concentrated in the 1–28 region that is also the region involved in metal ion binding. For this reason the effect of

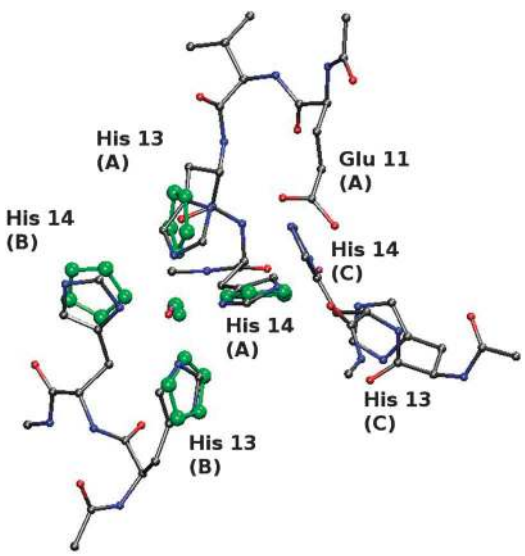

Fig. 7 Comparison between the atomic structure of the Zn_a site of the S4 model as it comes out of the fit (in green) and the S4 configuration from which the fitting procedure was started (in colors). Color code for the S4 model is as in Fig. 3 and only residues involved in Zn binding are displayed.

pH on amyloid deposit formation was monitored *in vitro*,[52] also in the presence of metal ions.[11] In this last study it is shown that the same mild acidic conditions observed *in vivo* increase the propensity for *in vitro* aggregation of Aβ(1–40/42) in the presence of different metal ions. In the absence of metal ions, the Aβ(1–40/42) aggregation becomes irreversible at pH = 5.5, a result somehow expected since the −2 charge of the 1–28 region can be partially neutralized by histidine protonation. Nevertheless, at pH = 6.6 aggregation with no metal ions is slower than in the presence of ions. As for the particular case of Zn, the binding to Aβ(1–40) does not occur at pH below 6.0, but the level of aggregation induced by Zn is almost invariant in the 6.2–8.5 pH range. Therefore, the conditions for Zn induced oligomerization are expected to be constant in the same pH range.

An interesting observation suggested by our simulation results is the similarity of the structure of the most stable among the models we have investigated, namely S4, with that of enzymes belonging to the Cu,Zn-SOD family. Indeed the Cu,Zn-SOD family contains enzymes with structures displaying high crowding of histidine sidechains around both, Cu and Zn, metal sites. In particular Cu is bound to four histidines, like Zn_a in the S4 model, while Zn is coordinated to three histidines and one Asp, in a configuration which corresponds to that of Zn_b in the S4 model, with Asp replaced by the almost equivalent Glu residue. The histidine crowding in SOD enzymes is helped by the presence of two metal ions bridged by the histidine sidechain in the unusual form of an imidazolate anion. The spectroscopic signatures of the active site of human Cu,Zn-SOD, with the deprotonated form of His_{63} (human SOD sequence) bridging Cu and Zn, are invariant in the pH range 5.0–10.5, while the same signatures become strongly pH dependent when His_{63} is mutated to Ala.[53] The dependence of the Cu(II)/Cu(I) standard reduction potential in human Cu,Zn-SOD is consistent with the presence of the bridging form of His_{63} in the pH range 5–9.[54] These results, together with a large amount of structural data,[55] show that a constrained geometry for the sites hosting metal ions in Cu,Zn-SOD strongly assists the stability of the imidazolate anion in a pH range including mild acidic conditions.

One may object to this conclusion that it has been recently shown by[29] that, after fully replacing Cu with Zn in the human SOD1 enzyme, the Zn ion located in the Cu site (Zn_{Cu}, equivalent to our Zn_a) loses the bond with the bridged histidine. It should be noted, however, that when the bridging histidine detaches at its place an oxygen from a sulfate binds Zn. Thus in our opinion the system studied in that paper cannot be directly compared to our S4 model, because of the strong influence on the metal environment coming from anion binding to metal sites. Fortunately, however, there exist in the literature data on the Cu,Zn-SOD with Cu in the reduced form and in the absence of metal binding anions. This system is quite interesting to compare with ours because the reduced Cu is isoelectronic to Zn. Indeed in ref. 56 and 57 where the Cu reduced SOD was crystalized the stability of the Cu–His–Zn bridge was shown to be preserved.

The similarity of the Zn coordination topology in model S4 with that of Cu,Zn-SOD is particularly remarkable if one observes that our construction of the S4 assembly as a model of Zn induced Aβ oligomers is completely independent from all the reported Cu,Zn-SOD structures. The topology of the initial S4 model was dictated by the binding of $Glu_{11}^{(A)}$, $His_{14}^{(A)}$ and the two water molecules to Zn_b, as it has been obtained in the final S3 structure (see the S3 right panel in Fig. 3). The relative position of $Glu_{11}^{(A)}$ with respect to $His_{14}^{(A)}$, very similar to that of Asp_{81} with respect to His_{61} in Cu,Zn-SOD (bovine SOD sequence), is the building block for the stable binding of chain C to Zn_b and for the stabilization of the S4 oligomer.

5 Conclusions

The electrostatic interactions between positively and negatively charged residues largely contribute in determining the mutual orientation of two approaching peptides and are thus important in providing the seeds for oligomer formation and their aggregation into larger assemblies. However, in the presence of transition metal ions, the coordination chemistry of the latter competes with the less specific electrostatic interactions between the peptide chain. In this work, by combining XAS and first-principle simulation results, we are able to take into account, in a consistent way, both types of interactions that span significantly different length scales. In fact, although, as already remarked in the Introduction, the short range sensitivity of the XAS technique allows us to identify at atomic resolution the structure around the absorber (in our case Zn) within a sphere of 5–6 Å, this knowledge is not enough to fully understand the role played by the metal in the complicated peptide aggregation mechanism. For this purpose, also the reconstruction of the system structure at distances larger than 6 Å is necessary. This is exactly what we provided with our first-principle, semiempirical and empirical simulations.

Indeed, the simulation results we have presented in the previous sections have lead us to the conclusions which we may summarize as follows.

(1) We have been able to construct stable Zn–Aβ-peptide sites (models S3 and S4 in Fig. 2, respectively) in which two peptides are bridged by a Zn ion (Zn_a) in a four histidine coordination mode.

(2) In the case of the S3 model a second Zn (Zn_b) is somewhat *ad hoc* introduced to ensure the stability of the configuration under CP-MD simulations. The four histidine coordinated Zn_a site is compatible with experimental results.

(3) A more realistic structure (model S4) has been constructed by adding a third peptide (peptide C in Fig. 2) to the system in a topology dictated by $Glu_{11}^{(A)}$, $His_{14}^{(A)}$ and water coordination to Zn in model S3. The S4 model, besides yielding a very good fit to XAS data, provides the geometric and chemical constraints that make both Zn sites structurally stable (see last row in Table 1).

Together with the remark that similar Zn–imidazolate–Zn coordination is observed in Zn imidazolate frameworks (ZIF) and in the Cu,Zn-SOD enzyme even at the mild acidic pH compatible with the acidosis observed in AD, the interesting conclusion we can draw is that in all these instances, *i.e.* ZIF, Cu,Zn-SOD and S4 model, the crowding of imidazolyl groups is helped by the presence of two metal ions bridged by the imidazolyl group in the unusual form of an imidazolate.

The relevance of the work presented in this paper comes from the observation that only on the basis of the quality of

the XAS fits displayed in Fig. 4 it would be impossible to choose among the various models we have considered and thus identify the structure of the first β-amyloid aggregates that can possibly form in the presence of metals. A careful study of the stability of small oligomeric assemblies is necessary. The aim of this paper was precisely to present a combined empirical and first-principle computational strategy by which the mechanical stability of different models can be studied. The application of this approach to the case of Aβ-peptides in the presence of Zn has lead us to the identification of a very peculiar arrangement of Zn ions and peptides whose stability largely depends on the formation of a Zn–His–Zn bridge assisted by an unusual deprotonated imidazole ring (imidazolate), very much like the one it is found in Cu,Zn-SOD even at mild acidic conditions.

Acknowledgements

All the computational work has been performed within the DEISA Extreme Computing Initiative (DECI), project BiCaPS (2008–2009) and the HCH03 project of the John von Neumann Institute for Computing (2009–2010). Partial financial support from INFN TO61 project and PRIN project 20083Y34Y7 is acknowledged.

References

1 S. B. Prusiner, *N. Engl. J. Med.*, 2001, **344**, 1516–1526.
2 M. B. Pepys, *Philos. Trans. R. Soc. London, Ser. B*, 2001, **356**, 203–210.
3 M. A. Lovell, J. D. Robertson, W. J. Teesdale, J. L. Campbell and W. R. Markesbery, *J. Neurol. Sci.*, 1998, **158**, 47–52.
4 M. A. Smith, P. L. Harris, L. M. Sayre and G. Perry, *Proc. Natl. Acad. Sci. U. S. A.*, 1997, **94**, 9866–9868.
5 A. I. Bush, *Trends Neurosci.*, 2003, **26**, 207–214.
6 K. J. Barnham, C. L. Masters and A. I. Bush, *Nat. Rev. Drug Discovery*, 2004, **3**, 205–214.
7 F. Stellato, G. Menestrina, M. Della Serra, C. Potrich, W. Tomazzolli, R. Meyer-Klaucke and S. Morante, *Eur. Biophys. J.*, 2006, **35**, 340–351.
8 V. Minicozzi, F. Stellato, M. Comai, M. Dalla Serra, C. Potrich, W. Meyer-Klaucke and S. Morante, *J. Biol. Chem.*, 2008, **283**, 10784–10792.
9 S. Morante, *Curr. Alzheimer Res.*, 2008, **5**, 508–524.
10 C. J. Maynard, A. I. Bush, C. L. Masters, R. Cappai and Q.-X. Lin, *Int. J. Exp. Pathol.*, 2005, **86**, 147–159.
11 C. S. Atwood, R. D. Moir, X. Huang, R. C. Scarpa, N. M. Bacarra, D. M. Romano, M. A. Hartshorn, R. E. Tanzi and A. I. Bush, *J. Biol. Chem.*, 1998, **273**, 12817–12826.
12 C. S. Atwood, R. C. Scarpa, X. Huang, R. D. Moir, W. D. Jones, D. P. Fairlie, R. E. Tanzi and A. I. Bush, *J. Neurochem.*, 2000, **75**, 1219–1233.
13 C. D. Syme and J. H. Viles, *Biochim. Biophys. Acta, Proteins Proteomics*, 2006, **1764**, 246–256.
14 P. Faller and C. Hureau, *Dalton Trans.*, 2009, 1080–1094.
15 Y. Mantri, M. Fioroni and M. H. Baik, *JBIC, J. Biol. Inorg. Chem.*, 2009, **13**, 1197–1204.
16 D. F. Raffa, R. Gomez-Balderas, P. Brunelle, G. A. Rickard and A. Rauk, *JBIC, J. Biol. Inorg. Chem.*, 2005, **10**, 887–902.
17 S. Furlan and G. La Penna, *Phys. Chem. Chem. Phys.*, 2009, **11**, 6468–6481.
18 T. Miura, K. Suzuki, N. Kohata and H. Takeuchi, *Biochemistry*, 2000, **39**, 7024–7031.
19 J. Danielsson, R. Pierattelli, L. Banci and A. Gräslund, *FEBS J.*, 2007, **274**, 46–59.
20 E. D. Walter, D. J. Stevens, M. P. Visconte and G. L. Millhauser, *J. Am. Chem. Soc.*, 2007, **129**, 15440–15441.
21 F. Stellato, A. Spevacek, O. Proux, G. L. Millhauser and S. Morante, *Eur. Biophys. J.*, 2011, **40**, 1259–1270.
22 J. Dong, J. E. Shokes, R. A. Scott and D. G. Lynn, *J. Am. Chem. Soc.*, 2006, **128**, 3540–3542.
23 S. Zirah, S. A. Kozin, A. K. Mazur, A. Blond, M. Cheminant, I. Ségalas-Milazzo, P. Debey and S. Rebuffat, *J. Biol. Chem.*, 2006, **281**, 2151–2161.
24 S. Karlin and Z.-Y. Zhu, *Proc. Natl. Acad. Sci. U. S. A.*, 1997, **94**, 14231–14236.
25 M. B. Peters, Y. Yang, B. Wang, L. Füsti-Molnár, M. N. Weaver and K. M. J. Merz, *J. Chem. Theory Comput.*, 2010, **6**, 2935–2947.
26 A. Teplyakov, G. Obmolova, P. P. Khil, A. J. Howard, R. D. Camerini-Otero and G. L. Gilliland, *Proteins: Struct., Funct., Genet.*, 2003, **51**, 315–318.
27 D. King, L. Zhang, L. Guarente and R. Marmorstein, *Nat. Struct. Biol.*, 1999, **6**, 64–71.
28 X. Siebert, B. A. Eipper, R. E. Mains, S. Prigge, N. J. Blackburn and L. M. Amzel, *Biophys. J.*, 2005, **89**, 3312–3319.
29 R. W. Strange, S. V. Antonyuk, M. A. Hough, P. A. Doucette, J. S. Valentine and S. S. Hasnain, *J. Mol. Biol.*, 2006, **356**, 1152–1162.
30 F. H. Allen, *Acta Crystallogr., Sect. B: Struct. Sci.*, 2002, **58**, 380–388.
31 C. Bear, K. A. Duggan and H. Freeman, *Acta Crystallogr., Sect. B: Struct. Crystallogr. Cryst. Chem.*, 1975, **31**, 2713–2715.
32 H. Xiaochun, L. Dan, T. Yexiang and C. Xiaoming, *Acta Scient. Nat. Univ. Sunyatseni*, 1998, **37**, 55–56.
33 R. Banerjee, A. Phan, B. Wang, C. Knobler, H. Furukawa, M. O'Keeffe and O. M. Yaghi, *Science*, 2008, **319**, 939–943.
34 N. Binsted, *EXCURV98*, CCLRC Daresbury Laboratory, Warrington, Cheshire, UK, 1998.
35 W. Humphrey, A. Dalke and K. Schulten, *J. Mol. Graphics*, 1996, **14**, 33–38, http://www.ks.uiuc.edu/Research/vmd.
36 W. D. Cornell, P. Cieplak, C. I. Bayly, I. R. Gould, K. M. J. Merz, D. M. Ferguson, D. C. Spellmeyer, T. Fox, J. W. Caldwell and P. A. Kollman, *J. Am. Chem. Soc.*, 1995, **117**, 5179–5197.
37 Y.-P. Pang, K. Xu, J. El Yazal and F. G. Prendergast, *Protein Sci.*, 2000, **9**, 1857–1865.
38 J. C. Phillips, R. Braun, W. Wang, J. Gumbart, E. Tajkhorshid, E. Villa, C. Chipot, R. D. Skeel, L. Kalé and K. Schulten, *J. Comput. Chem.*, 2005, **26**, 1781–1802, http://www.ks.uiuc.edu/Research/namd.
39 G. La Penna, S. Morante, A. Perico and G. C. Rossi, *J. Chem. Phys.*, 2004, **121**, 10725–10741.
40 W. L. Jorgensen, J. Chandrasekhar, J. D. Madura, R. W. Impey and M. J. Klein, *J. Chem. Phys.*, 1983, **79**, 926–935.
41 H. J. C. Berendsen, J. P. M. Postma, W. F. van Gunsteren, A. Di Nola and J. R. Haak, *J. Chem. Phys.*, 1984, **81**, 3684–3690.
42 B. Aradi, B. Hourahine and T. Frauenheim, *J. Phys. Chem. A*, 2007, **111**, 5678–5684, http://www.dftb-plus.info.
43 N. H. Moreira, G. Dolgonos, B. Aradi, A. L. da Rosa and T. Frauenheim, *J. Chem. Theory Comput.*, 2009, **5**, 605–614.
44 R. Car and M. Parrinello, *Phys. Rev. Lett.*, 1985, **55**, 2471–2474.
45 V. Minicozzi and S. Morante, *Int. J. Quantum Chem.*, 2010, **110**, 656–680.
46 P. Giannozzi, S. Baroni, N. Bonini, M. Calandra, R. Car, C. Cavazzoni, D. Ceresoli, G. L. Chiarotti, M. Cococcioni, I. Dabo, A. Dal Corso, S. de Gironcoli, S. Fabris, G. Fratesi, R. Gebauer, U. Gerstmann, C. Gougoussis, A. Kokalj, M. Lazzeri, L. Martin-Samos, N. Marzari, F. Mauri, R. Mazzarello, S. Paolini, A. Pasquarello, L. Paulatto, C. Sbraccia, S. Scandolo, G. Sclauzero, A. P. Seitsonen, A. Smogunov, U. Paolo and R. M. Wentzcovitch, *J. Phys.: Condens. Matter*, 2009, **21**, 395502, http://www.quantum-espresso.org.
47 D. Vanderbilt, *Phys. Rev. B: Condens. Matter*, 1990, **41**, 7892–7895.
48 P. Giannozzi, F. De Angelis and R. Car, *J. Chem. Phys.*, 2004, **120**, 5903–5915.
49 J. P. Perdew, K. Burke and M. Ernzerhof, *Phys. Rev. Lett.*, 1996, **77**, 3865–3868.
50 F. Guerrieri, V. Minicozzi, S. Morante, G. Rossi, S. Furlan and G. La Penna, *JBIC, J. Biol. Inorg. Chem.*, 2009, **14**, 361–374.
51 C. M. Yates, J. Butterworth, M. C. Tennant and A. Gordon, *J. Neurochem.*, 1990, **55**, 1624–1630.

52 C. Soto, M. C. Brañes, J. Alvarez and N. C. Inestrosa, *J. Neurochem.*, 1994, **63**, 1191–1198.
53 J. A. Graden, L. M. Ellerby, J. A. Roe and J. S. Valentine, *J. Am. Chem. Soc.*, 1994, **116**, 9743–9744.
54 H. A. Azab, L. Banci, M. Borsari, C. Luchinat, M. Sola and M. S. Viezzoli, *Inorg. Chem.*, 1992, **31**, 4649–4655.
55 L. M. Ellerby, D. E. Cabelli, J. A. Graden and J. S. Valentine, *J. Am. Chem. Soc.*, 1996, **118**, 6556–6561.
56 W. R. Rypniewski, S. Mangani, B. Bruni, P. L. Orioli, M. Casati and K. S. Wilson, *J. Mol. Biol.*, 1995, **251**, 282–296.
57 M. Ferraroni, W. R. Rypniewski, B. Bruni, P. Orioli and S. Mangani, *JBIC, J. Biol. Inorg. Chem.*, 1998, **3**, 411–422.